Journal of Inorganic and General Chemistry
ZAAC
Zeitschrift für anorganische und allgemeine Chemie
doi.org/10.1002/zaac.202100245
ARTICLE

Metal complexes of Tridentate Schiff base: Synthesis, Characterization, Biological Activity and Molecular Docking Studies with COVID-19 Protein Receptor

Gehad G. Mohamed,[a] M. M. Omar,[a] and Yasmin M. Ahmed*[a]

Mononuclear chelates of Cr(III), Mn(II), Fe(III), Ni(II), Cu(II), Zn(II) and Cd(II) resulted from new tridentate Schiff base ligand, 4-((1-(5-acetyl-2,4-dihydroxyphenyl)ethylidene)amino)-1,5-dimethyl-2-phenyl-1H-pyrazol-3(2H)-one, were synthesized. Metal to ligand ratio was found to be1:1, which was revealed via elemental analysis and characterized via various spectroscopic tools. IR has point out that the coordination of the ligand towards the metal ions was carried out via NOO donor atoms. UV-Vis, ^{1}H NMR spectral data, molar conductivity measurements, BET surface area, melting points and theoretically through density function theory were used such as characterizing techniques in supporting further interpretation of the complexes structures. The complexes were octahedral except Cu(II) and Ni(II) complexes were tetrahedral as suggested from the magnetic moment measurement. The complexes were found to have surface area, pore volume and particle radius of 23–176 $m^2 g^{-1}$, 0.02-0.33 cc/g and 8.71-4.32 nm, respectively, as pointed out from BET measurement. Schiff base ligand and metal complexes were tested *in vitro* to estimate their antimicrobial activity opposed to Gram-negative and Gram-positive bacterial and fungal organisms. MOE 2008 was used headed for screen potential drugs with molecular docking by the protein sites of new coronavirus and the study was constructed to molecular docking without validation through MD simulations.

1. Introduction

Schiff bases derived from the condensation of an amino and a carbonyl compound, form an important class of ligands that have the propensity to bind almost all metal ions via azomethine nitrogen.[1] The chemistry of Schiff bases has been discussed extensively over the past few decades due to the most versatile starting compounds in coordination chemistry, exhibit significant biological applications including antifungal, antibacterial, antiviral, anticancer and antioxidant activities.[2,3]

The excessive use of antimicrobial has been a major factor in the rise of drug-resistant microbes, which remain a leading cause of death worldwide. Because of a lack of effective treatments, microbial infections cause serious problems to humankind. Therefore, to overcome the growing resistance of antimicrobial agents, researchers are developing new classes of antimicrobial drugs with adequate mechanisms. In recent years, transition metal complexes[4] have many clinical, biochemical, and pharmacological properties.[5]

A wide variety of pharmaceutical activities are available at different Schiff base metal complexes. For example, as a result of their biological properties, transition metal complexes with "N" and "O" Schiff base ligands are very important in supporting antibacterial, anticonvulsant, antifungal, anti-inflammatory, antioxidative, antitumoral, analgesic and anthelmintic examples.[6]

[a] *G. G. Mohamed, M. M. Omar, Y. M. Ahmed*
Chemistry Department, Faculty of Science, Cairo University, Giza, 12613, Egypt
E-mail: yassmine@sci.cu.edu.eg

Supporting information for this article is available on the WWW under https://doi.org/10.1002/zaac.202100245

The bifunctional carbonyl compound namely 4,6-diacetylresorcinol (DAR) serves as precursor for the building of tridentate ligands. Over the past few years, 4,6-diacetylresorcinol had also received much attention towards the biological applications as well as the coordination chemistry.[7,8]

4-Aminoantipyrine is a pyrazalone derivative, it has shown wide range of biological activities such as antimicrobial activity, analgesic, antiviral and also used as precursors in the synthesis of bioactive compounds i.e. β-lactams.[9] The unwanted COVID-19 outbreak driven by this highly infectious virus SARS-CoV-2 has spread its tentacles over the entire world and has taken millions of people under its cover. Everyday huge number of people loses their lives due to this deadly disease.[10] The ongoing 2019 coronavirus (COVID-19), allegedly caused by so-called severe acute coronavirus 2 (SARS-CoV-2) syndrome, is a significant cause of global serious health problems.

People commit themselves to staying at home either because of a compulsory local lock-out guideline or because they are afraid that there is an apparently endless pandemic that should protect themselves. This is highly infecting viral infection from China has first been officially reported in most parts of the world on 31 December 2019[11,12].

In addition to their metallic complexes, this work aimed to synthesize the new Schiff base ligand. Many characterization tests have described in order to emphasize the structures of the complexes. Apart from anti-breast cancer activities, *in vitro* antimicrobial was also screened. The binding affinity of the synthesized compounds towards the SARS-CoV-2 main protease with UAW247 crystal-structure inhibitor (PDB-ID: 6XBH) was examined by molecular docking study. Thus, docking research was aimed at this target. Based on results of molecular docking, the scoring function have calculated indicating the enthalpy

contribution to the value of free binding energy (Affinity DG) for the best conformational positions; values of free binding energy and binding constants (EDoc kcal/mol and Ki uM (micromolar)) for a fixed conformational position of the ligand allowed to measure the stability of complexes formed between ligand and complexes and the corresponding protein target.[10]

2. Results and discussion

2.1 Characterization of Schiff base and metal complexes

Elemental analyses are conducted on the new Schiff base ligand, H_2L. In addition to the melting points, the results of elemental analyses (N, H and C) are present in Table 1. The results obtained are consistent with the results calculated from the proposed formula. The sharp melting points represent the purity of the Schiff base ligand and complexes preparation. The preparation scheme for the Schiff base is set out in Scheme1. Additionally, the structure of this Schiff base is confirmed by IR and ^{1}H NMR spectral analyses which will be discussed later in detail with the metal complexes.[15]

The new Schiff base ligand has an orange color and stable at room temperature. In DMF and DMSO solvents, it was soluble. The results obtained were in due agreement, depending on those determined in accordance with the proposed formula.

The structure of the Schiff base ligand was shown in scheme 1The metal-to-ligand ratio in all complexes which were achieved by estimating the carbon, hydrogen, nitrogen, and metal contents was supposed to be 1:1 (Table 1) and to be MH_2L type. The results of the experimental elemental analyses for the complexes were close to the theoretical calculations (Table 1) depending on the formula proposed.[16]

The structures of the metal complexes of the tridentate Schiff base ligand (H_2L) were characterized through elemental analyses, molar conductivity, IR, ^{1}H NMR, UV–Vis, mass and thermal analyses and their suggested structures were given in Figure 1.

2.2 Composition and structure of Schiff base and its complexes

2.2.1 Infrared spectra

The data of the IR spectra of Schiff base ligand (H_2L) and its mononuclear metal complexes were listed in Table (2).[14] H_2L

Table 1. Analytical and physical data of Schiff base ligand (H_2L) and its metal complexes.

Compound (Molecular Formula)	Colour (%yield)	M.p. (°C)	% Found (Calcd.) C	H	N	M	Λ_m $\Omega^{-1}mol^{-1}$ cm^2	μ_{eff} (BM)
H_2L	orange (92)	190	66.39 (66.42)	5.49 (5.53)	11.01 (11.07)	–	–	–
$[Cr(H_2L)(H_2O)_2Cl]Cl_2\cdot 2H_2O$	yellow (85)	>300	41.28 (41.34)	4.64 (4.76)	6.72 (6.89)	8.41 (8.53)	113	3.99
$[Mn(H_2L)(H_2O)_2Cl]Cl\cdot 2H_2O$	brown (84)	206	43.18 (43.66)	4.99 (5.02)	7.20 (7.27)	9.39 (9.52)	63	5.41
$[Fe(H_2L)(H_2O)_2Cl]Cl_2$	brown (83)	>300	43.37 (43.61)	4.29 (4.33)	7.19 (7.27)	9.56 (9.69)	103	5.28
$[Ni(H_2L)(H_2O)]Cl_2\cdot 4H_2O$	green (80)	>300	42.01 (42.06)	5.07 (5.17)	7.00 (7.01)	9.71 (9.85)	107	4.39
$[Cu(H_2L)Cl]Cl\cdot 2H_2O$	Greenish blue (86)	>300	45.73 (45.82)	4.43 (4.55)	7.22 (7.64)	11.18 (11.55)	74	2.8
$[Zn(H_2L)(H_2O)Cl_2]\cdot 2H_2O$	Dark brown (84)	169	43.83 (44.23)	4.63 (4.74)	7.30 (7.37)	11.37 (11.41)	24	Diamagnetic
$[Cd(H_2L)(H_2O)Cl_2]$	brown (85)	158	43.25 (43.39)	3.78 (3.96)	7.21 (7.23)	19.19 (19.35)	9	Diamagnetic

Table 2. IR spectra of H_2L ligand and its metal complexes.

Assignment	ν(OH) phenolic and H_2O	ν(C=N) azomethine	ν(C=O) resorcinol	ν(C=O) antipyrine	ρr(H_2O) and ρw(H_2O).	ν(M–O)	ν(M–N)
H_2L	–	1589m	1652br		–	–	–
$[Cr(H_2L)(H_2O)_2Cl]Cl_2\cdot 2H_2O$	3424br,3148br	1531sh	1643 m	1620s	757, 698	575	452
$[Mn(H_2L)(H_2O)_2Cl]Cl\cdot 2H_2O$	3428br,3192br	1560s	1636br		839, 666	578	421
$[Fe(H_2L)(H_2O)_2Cl]Cl_2$	3417br,3165br	1539m	1648sh	1595s	840, 692	546	453
$[Ni(H_2L)(H_2O)]Cl_2\cdot 4H_2O$	3429br	1550s	1626br		876, 720	591	443
$[Cu(H_2L)Cl]Cl\cdot 2H_2O$	3425br,3244br	1541sh	1630sh	1601s	836, 694	599	429
$[Zn(H_2L)(H_2O)Cl_2]\cdot 2H_2O$	3439br,3264br	1579s	1651sh	1620s	840, 699	579	459
$[Cd(H_2L)(H_2O)Cl_2]$	3421br	1587m	1652sh	1630s	889, 696	590	448

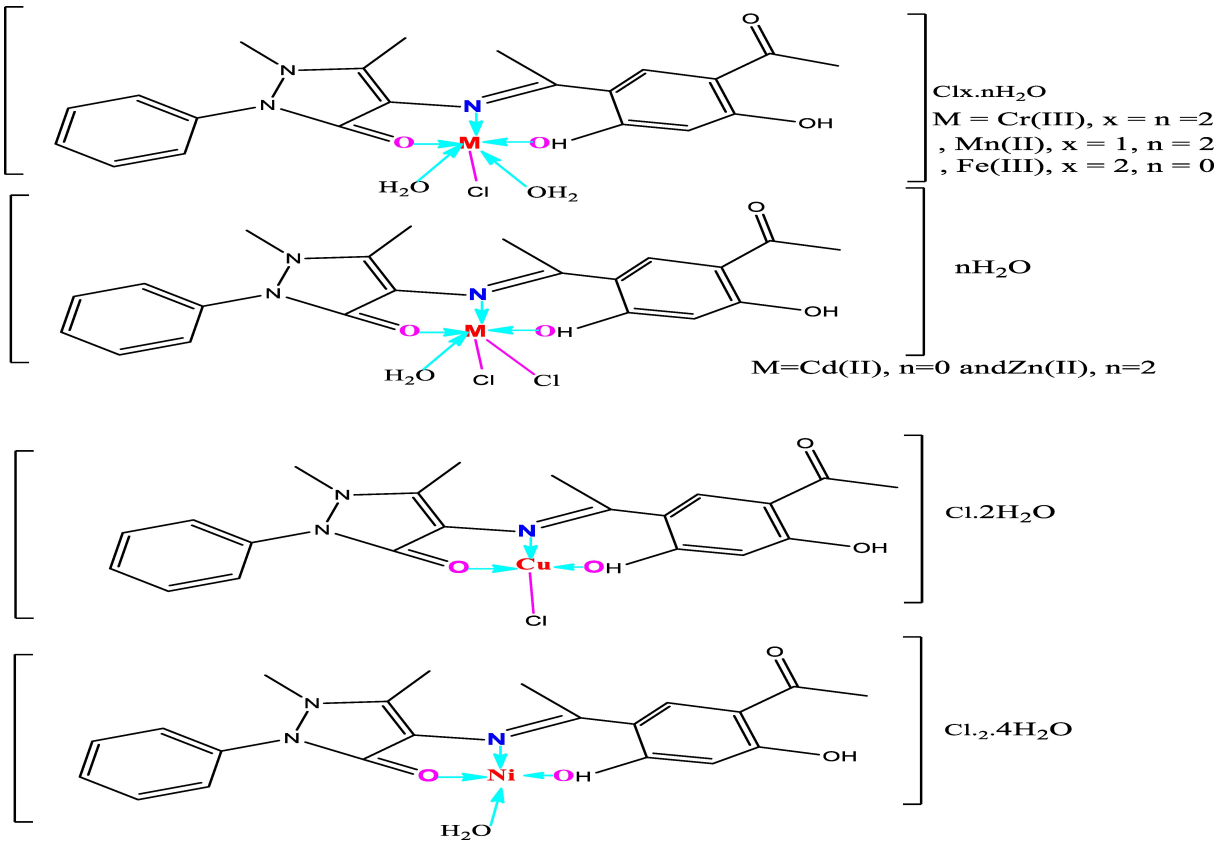

Figure 1. Structures of Schiff base metal complexes.

ligand showed an absence of the 4-aminoantipyrin NH_2 stretching band. Alternatively, a new strong and sharp vibration band was appeared at 1589 cm^{-1}attributable to the azomethine group, ν(C=N), indicating the formation of the Schiff base ligand (H_2L). IR spectra of the complexes exhibited shifts in the band related to the azomethine groups, ν(C=N), which refers to the coordination of this group to the metal ions.[19] The broad band of carbonyl groups, ν(C=O), of resorcinol and 4-aminoantipyrine, was appeared at 1652 cm^{-1}.[20] The IR spectra of the complexes showed two bands related to carbonyl of resorcinol and antipyrine in 1636–1652 and 1595–1636 cm^{-1}, respectively. The slight shift in the resorcinol carbonyl group can accounted to the formation of a hydrogen bond with the adjacent hydrogen. The apparent shift in the antipyrine carbonyl group may be attributed to its participation in metal ions coordination. This was confirmed by the appearance of the stretching vibrations of the M–N and M–O bands in 421–459 cm^{-1} and in 546–599 cm^{-1} regions, respectively.[19] The IR spectra of the complexes showed broad bands at 3148–3264 and 3417–3439 cm^{-1} which could be allocated to ν(OH) of water molecules and ν(OH) phenolic group. Also, the spectra showed peaks at 666–720 and 757–889 cm^{-1} due to the rocking (ρr(H_2O)) and wagging (ρw(H_2O)) vibrations of water molecules, respectively. However, a TG-DTG analysis can further confirm the presence of various types of water molecules.[17,18]

2.2.2 ^{1}H NMR spectral study

In addition to its purity, the ligand structure was supported by ^{1}H NMR spectral data (δ ppm) carried out for the free ligand using TMS (0 ppm) and DMSO-d_6 solvent. Two phenolic OH^a and OH^b protons, respectively, can be assigned to the signals seen at 16.10 and 16.73 ppm. Also, the free ligand spectrum (H_2L) showed a multiple signal at 6.27–8.41 ppm region that can be assigned to the aromatic protons (m,7H, Ar–H). The ligand spectrum showed overlapping singlets at 2.26-3.13 ppm for methyl protons (s, 12H, $4CH_3$).[11,14,18] The lack of a peak for the $–NH_2$ group at around 4 ppm indicated the production of the most wanted product.[22]

The ^{1}H NMR spectral (δ ppm) data of Cd(II) and Zn(II) complexes showed phenolic OH^a protons at 16.10 and 16.11 ppm and OH^b protons at 16.67 and 16.70 ppm for Cd(II) and Zn(II) complexes, respectively. The phenolic OH^b proton was slightly shifted from its position in the free ligand which indicated that OH^b participated in coordination to the metal ions without proton displacement. While the phenolic OH^a proton appeared in the same position of the free ligand confirming its non-involvement in chelate formation. In the aromatic region, the spectra showed overlapping signals at the range of 6.27–8.40 and 6.27–8.38 ppm for Zn(II) and Cd(II) complexes, respectively. The methyl protons were found in the aliphatic region (m, 12H, $4CH_3$) as overlapping singlet signals

observed in the range of 2.10–3.50 and 2.09–3.31 ppm for Cd(II) and Zn(II) complexes, respectively.[23]

The data of the ^{1}H NMR spectra of Schiff base ligand (H_2L) and its mononuclear metal complexes are shown in Figure 2.

2.2.3 Molar conductivity measurement

The molar conductivity of the metal complexes was determined with the aid of DMF as a solvent (Table1). The molar conductivity was found within the 9–113 $Ohm^{-1}cm^2mol^{-1}$ range. The molar conductivity values of the complexes showed their electrolytic nature except for the Zn(II) and Cd(II) complexes, which are non-electrolytes (Table 1).[24]

2.2.4 Electronic spectra and magnetic properties of prepared complexes

Magnetic susceptibility measurements and diffused reflectance spectral data were used to infer the structures of the complexes. The effective magnetic moment (μ_{eff}) values were also used to predict the geometry of complexes at room temperature.

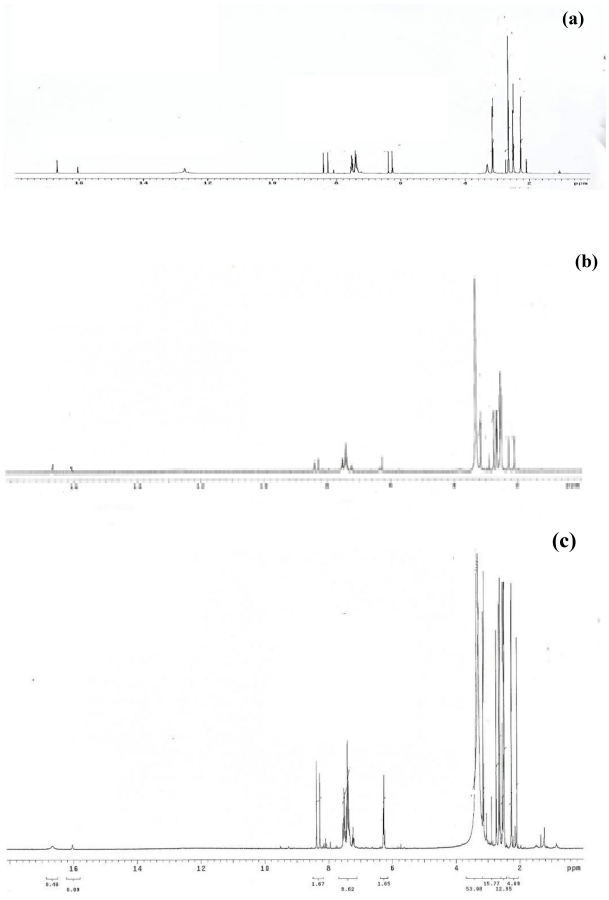

Figure 2. ^{1}H NMR spectra of (a) H_2L, (b) Zn(II) and (c) Cd(II) complexes.

The electronic spectra of the ligand and metal complexes were carried out in DMF as a solvent within the wavelength range from 200 to 700 nm. Only one high-intensity peak at 395 nm was detected in the UV-Vis spectrum of the prepared Schiff base ligand. This peak can be accounted to the $\pi\rightarrow\pi^*$ transition of the azomethine group. This peak was shifted in the spectra of complexes to lower wavelengths in the range of 337–378 nm. This shift can attribute to the coordination of the azomethine group in the Schiff base ligand to metal ions.[25]

The Cr(III) complex was equivalent to three unpaired electrons, i.e. has μ_{eff} 3.99 B.M. corresponding to high-spin chromium(III) octahedral complexes.[25,26] The Cr(III) complex displays bands at 17,953, 25,169, 26,436, and 39,525 cm^{-1}, respectively. These bands may be ascribed to $^4B_{1g}\rightarrow{}^4E_g$, $^4B_{1g}\rightarrow{}^4B_{2g}$, $^4B_{1g}\rightarrow{}^4Eb_g$ and $^4B_{1g}\rightarrow{}^4A_{1g}$ transitions, respectively, resulting from an increase in the energy degeneration of orbital triplet in octahedral geometry.[25,26]

The high-spin octahedral Mn(II) complex has magnetic moment equivalent to five unpaired electrons (i.e., 5.41 B.M). The diffused reflectance spectrum of the Mn(II) complex displayed three bands at 17,801, 21,942 and 24,492 cm^{-1}. These bands may be attributed to $^6A_{1g}\rightarrow{}^4T_{1g}(G)$; $^6A_{1g}\rightarrow{}^4T_{2g}(G)$ and $^6A_{1g}\rightarrow{}^4T_{1g}(P)$ transitions, respectively. The ligand field bands and magnetic moment value therefore support an octahedral geometry of the Mn(II) complex.[14,27]

The Fe(III) complex had magnetic moment value of 5.28 B.M. ascribed for high-spin octahedral Fe(III) complexes.[14] Three bands were observed in the solid reflectance spectrum at 22,127, 19,897 and 17,035 cm^{-1}. These bands may be ascribed for $^4T_{2g}(G)\rightarrow{}^6A_{1g}$, $^4T_{2g}(G)\rightarrow{}^6A_{1g}$ and $^4T_{1g}(D)\rightarrow{}^6A_{1g}$ transitions, respectively.[14] Ni(II) complex had magnetic moment of 3.33 B.M which equivalent to two unpaired electrons. Bands found in the diffused reflectance spectrum at 12,219, 17,002 and 23,122 cm^{-1} were accounted for $^3A_2(F)\rightarrow{}^3T_2(F)$, $^3A_2(F)\rightarrow{}^3T_1(F)$ and $^3A_2(F)\rightarrow{}^3T_1(P)$ transitions, respectively. The bands position and magnetic moment value ascertained the tetrahedral geometry[26,28].

Diffused reflectance spectrum of the Cu(II) complex displays bands at 10,842, 19,765 and 29,928 cm^{-1}. First two bands may be ascribed to the transitions: $^2B_{1g}\rightarrow{}^2A_{1g}$ (dx^2-$y^2\rightarrow dz^2$) and $^2B_{1g}\rightarrow{}^2B_{2g}$ (dx^2-$y^2\rightarrow dzy$), respectively. The third band may be due to charge transfer. Also, the magnetic moment value of the Cu(II) complex is 2.80 B.M. which equivalent to the presence of one unpaired electron which is consistent with tetrahedral geometry. This indicated the formation of tetrahedral geometry of the complex.[14,26,28,29]

In general, octahedral-geometry was proposed for Zn(II) and Cd(II) complexes and due to its fully filled d^{10} orbital, there were no d-d electronic transitions.[14,28]

2.2.5 Geometry optimization

Figure 3 shows the fully optimized geometries of the H_2L ligand plus its Cd(II) complex. Distorted octahedral geometry around the Cd(II) ion was suggested as deduced from the selected bond lengths and bond angles calculated for Cd(II) complex

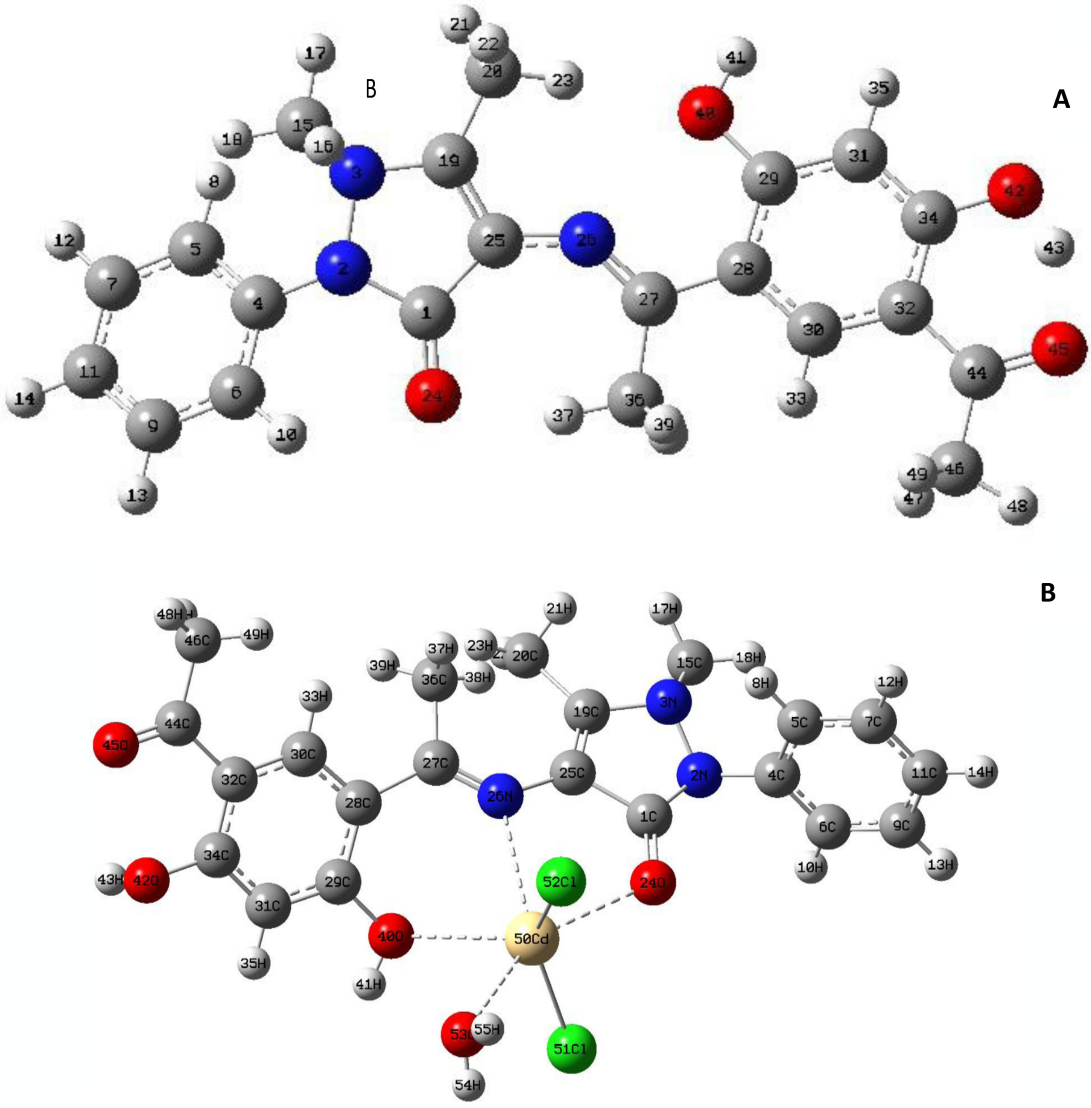

Figure 3. The optimized structures of (A) H_2L and (B) Cd(II) complex.

and Schiff base ligand (Table 3). The bond lengths of C(25)–N-N(26), C(1)–O(24) and C(29)–O(40) were 1.47, 1.25 and 1.43, respectively, in the ligand. They showed a small elongation upon coordination to Cd(II) ion and found to be 1.50, 1.33 and 1.45 A°, respectively. In the Cd(II) complex, the ligand (H_2L) coordinated by azomethine nitrogen, carbonyl oxygen and phenolic oxygen, while two chloride ions and coordinated water oxygen took up other three positions. As previously stated, the bond angles in the Cd(II) coordination sphere were investigated the octahedral geometry. Intramolecular hydrogen connections can be attributed to the reduction of the metal chloride angles.[14,11,30]

2.2.6 Molecular electrostatic potential (MEP)

To study the reactions, electrostatic potential V(r) maps were calculated which are known for the identification of the electronic charge distribution around molecular surface and subsequently to predict the expected sites for the reactions. These graphs are calculated using the same set of bases as optimized. In this study, a 3D MEP map of the ligand and its Cd(II) complex was drawn (Figure 4). According to MEP, it can generally sort the red electronic-rich areas on the map (favorable for sites that are electrophilic attack). However, the electron-deficient area is blue (a favorable position for nucleophilic attack). But the green area points to the area of neutral electrostatic potential. H_2L is stable and has an approximately uniform charge density distribution. However, the two oxygen and nitrogen atoms are surrounded by a larger negatively charged surface, making these sites potentially more suitable for electrophilic attack (red). (Figure 4).[14]

In terms of electron density, the aromatic ring appears to be neutral. This potential distribution leads to the complexation reaction, which is further confirmed by the electrostatic potential distribution of the Cd(II) complex, where the largest

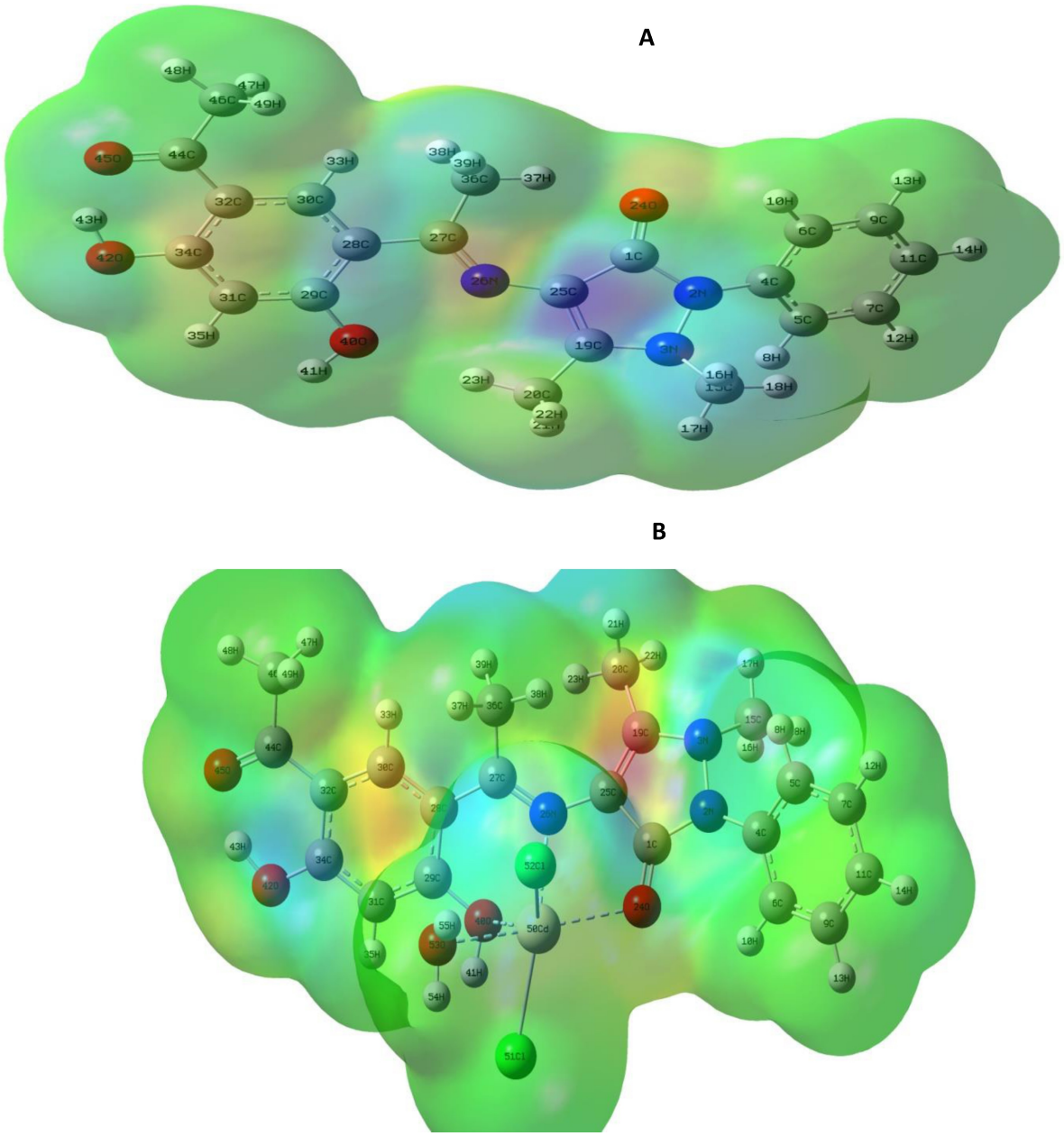

Figure 4. Molecular electrostatic potential map of (A) H_2Land (B)[Cd(H_2L)(H_2O)Cl_2]complex. The electron density isosurface is 0.004 a.u.

negative charge is surrounded by the metal center (Figure 4b). In addition to the increase of the electron negative capacity of oxygen and nitrogen in Cd(II) complex than free H_2L, the Mulliken electron negative is the favored location for electrical attacks with metal ion.[11,14,30]

2.2.7 Molecular parameters

In continuation to our work,[6] Table 3 lists the different geometrical parameters of the free H_2L ligand with its Cd(II) complex. It can conclude that, the Cd(II) complex displayed high dipole values compared to the free ligand. The main orbital elements participating in chemical stability were the highest occupied molecular orbital (HOMO) and the lowest unoccupied molecular orbital (LUMO). The HOMO is an electron donation capability, LUMO is an electron accepting device, it is an electron donation capability. It can assume from the achieved data that the HOMO and LUMO energies of Cd(II) complex were negative, and more negative than free H_2L, confirming lonely complex stability. The E_{HOMO} and E_{LUMO} values of Cd(II) complex have been calculated and show that the Cd(II)–H_2L bond strength is lower than the free ligand. The total energy of Cd(II) complex is larger than the free ligand, and the consistency of the solid lonely complex is highly evident. The little energy divide can be linked to a high chemical reactivity,

low kinetic stability, and the highly polarizing molecule mirror to active electronic charge transfer interaction. Azomethine nitrogen and oxygen were usually located at the HOMO levels of the ligand phenol groups, which indicated the preferred places of nuclear attack against the central metal atom. H_2L and its Cd(II) complex contains different optimized and quantum chemical parameters (Table 3).[11,13,14]

Table 3. The different optimized and quantum chemical parameters of H_2L and its Cd(II) complex.

Bond lengths (Å)	H_2L	$[Cd(H_2L)(H_2O)Cl_2]$
C(1)–N(2)	1.46	1.47
C(1)–O(24)	1.25	1.33
N(2)–N(3)	1.41	1.43
N(2)–C(4)	1.47	1.47
N(3)–C(15)	1.47	1.47
N(3)–C(19)	1.50	1.49
C(25)–N(26)	1.46	1.50
N(26)–C(27)	1.31	1.31
C(29)–O(40)	1.43	1.45
C(34)–O(42)	1.43	1.43
O(40)–H(41)	0.96	0.96
O(42)–H(43)	0.96	0.96
C(44)–O(45)	1.26	1.26
Cd(50)–Cl(51)	—	2.40
Cd(50)–Cl(52)	—	2.40
Cd(50)–O(53)	—	3.11
O(40)–Cd(50)	—	3.06
N(26)–Cd(50)	—	3.06
O(24)–Cd(50)	—	3.08
Bond angles (°)		
O(24)–Cd(50)–O(40)	—	114
O(24)–Cd(50)–Cl(52)	—	89
N(26)–Cd(50)–Cl(52)	—	93
O(40)–Cd(50)–Cl(51)	—	90
O(40)–Cd(50)–O(53)	—	94
Cl(51)–Cd(50)–O(53)	—	86
The calculated quantum chemical parameters		
E (a.u.)	−1270.99	−7705.93
Dipole moment (Debye)	4.60	13.75
E_{HOMO} (eV)	−5.51	−6.10
E_{LUMO} (eV)	−1.70	−2.30
Δ E (eV)	3.81	3.80
χ (eV)	−3.61	−4.20
η (eV)	1.91	1.90
σ $(eV)^{-1}$	0.52	0.53
Pi (eV)	3.61	4.20
S $(eV)^{-1}$	0.26	0.26
ω (eV)	3.41	4.64
$\triangle N_{max}$	1.89	−2.21

2.2.8 UV-Vis spectra

Explaining the photochemistry of transition metal compounds requires understanding the properties of molecular orbitals and appropriate excited states. Boundary orbitals play a relevant role in such systems because they control the electronic excitation and transition properties. With the help of TD-DFT calculations, the contribution of ligands and metal orbitals to molecular orbitals can be fed back. It is impractical to analyze all electronic transitions and orbitals; therefore, some restrictions are used. Due to the high accuracy and low computational cost of TD-DFT, it has become popular in the theoretical research of molecular electronic spectroscopy. At present, the exploration of the low-level excited state in the optimized ground state structure of H_2L and its Cd(II) complex has been carried out on the theoretical level of TD-DFT / B3LYP / LANL2DZ thirty singlet states. In Table 4, the experimental and theoretical electronic spectra are given. The TD-DFT calculation has been evaluated in the solvent background of N,N dimethylformamide and matched the experimental data.

Figure 5a, b shows the transition between the orbitals between the limits of the wavelength corresponding to the maximum intensity of the oscillator of the simulation results and the contemporary experimental observations. For example, the calculated peak for H_2L ligand obtained at 366 nm match to experimental peak at 395 nm. This transition has been majorly contributed from HOMO to LUMO transitions which were primarily $\pi \rightarrow \pi^*$ in nature. The various transitions and their experimental matching part of the free ligand and its Cd(II) complex have been summarized in Table 4.[11,13,14]

2.2.9 Thermogravimetric Analysis

Thermogravimetric analysis (TGA) of new Schiff base ligand and its metal complexes were carried out in nitrogen atmosphere at a heating rate of 10 °C /min from room temperature (30 °C) to 1000 °C.

The thermal stabilities of these nine compounds are slightly different. The thermal decomposition process of novel Schiff base ligand ($C_{21}H_{21}N_3O_4$), concerned three steps of weight loss, as shown in Table 5. A primal two step weight loss of 37.69% (calcd. mass loss 37.25%) is observed in the temperature range of 30 °C to 330 °C, on account of the decomposition of the $C_{10}H_{21}$ molecule. The last step shows a weight loss of about 60.17% (calcd. mass loss 62.75%) in the range of 330–900 °C, on account of the decomposition of the $C_{11}N_3O_4$ molecule.

The $[Cr(H_2L)(H_2O)_2Cl]Cl_2 \cdot 2H_2O$ complex concerned four procedures of weight loss, as shown in Table 5. A primal weight

Table 4. Main calculated optical transition with composite ion in terms of molecular orbitals.

Compound	Transition	Excitation energy (ev)	λ_{max} Calc. (nm)	λ_{max} exp. (nm)	Oscillating strength
H_2L	HOMO LUMO	3.39	366	395	0.147
$[Cd(H_2L)Cl_2(H_2O)]$	HOMO LUMO	3.42	363	340	0.142

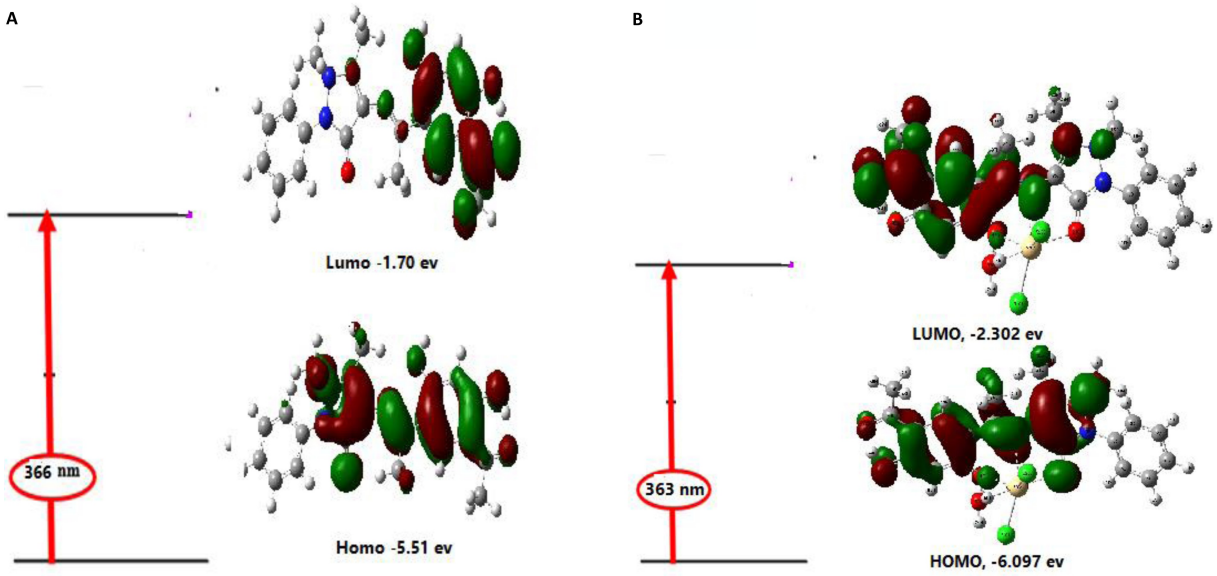

Figure 5. a) Theoretical electronic absorption transitions for H_2L in ethanol solvent. b) Theoretical electronic absorption transitions for Cd(II) complex in DMF solvent.

Table 5. Thermoanalytical results (TG and DTG) of Schiff base ligand (H_2L) and its metal complexes.

Complex	TG range (°C)	DTG_{max} (°C)	n*	Mass loss Total mass loss Estim (Calcd) %	Assignment	Residues
H_2L	30–330	195, 255	2	37.69 (37.25)	- Loss of $C_{10}H_{21}$.	
	330–900	400	1	60.17 (62.75)	- Loss of $C_{11}N_3O_4$.	
				97.69 (100.00)		
$[Cr(H_2L)(H_2O)_2\ Cl]Cl_2\cdot 2H_2O$	30–120	66	1	5.64 (5.90)	- Loss of $2H_2O$.	$^1/_2Cr_2O_3 + 5C$
	120–900	218, 700, 810	3	69,70 (71.31)	- Loss of $1.5Cl_2$, $2H_2O$	
				75.34 (77.21)	and $C_{16}H_{22}N_3O_{2.5}$.	
$[Mn(H_2L)(H_2O)_2Cl]Cl\cdot 2H_2O$	30–375	71, 125, 155	3	34.50 (34.81)	- Loss of Cl_2,$4H_2O$, C_4H_{10}.	$MnO + 5C$
	375–900	379, 812	2	41.62 (42.43)	- Loss of $C_{12}H_{11}N_3O_3$.	
				76.12 (77.24)		
$[Fe(H_2L)(H_2O)_2Cl]Cl_2$	30–900	139, 204	2	78.15 (77.78)	- Loss of $1.5Cl_2$, $2H_2O$	$^1/_2Fe_2O_3 + 4C$
				78.15 (77.78)	and $C_{17}H_{21}N_3O_{2.5}$.	
$[Ni(H_2L)(H_2O)]Cl_2\cdot 4H_2O$	30–250	73, 157	2	27.29 (26.87)	- Loss of $5H_2O$, Cl_2.	$NiO + 5C$
	250–900	183, 424	2	50.91 (50.74)	- Loss of $C_{16}H_{21}N_3O_3$.	
				78.2 (77.61)		
$[Cu(H_2L)Cl]Cl\cdot 2H_2O$	30–135	68	1	6.56 (6.55)	- Loss of $2H_2O$.	$CuO + 4C$
	135–900	169, 270, 550	3	69.02 (70.19)	- Loss of Cl_2, $C_{17}H_{21}N_3O_3$.	
				75.58 (76.74)		
$[Zn(H_2L)(H_2O)Cl_2]\cdot 2H_2O$	30–180	61, 155	2	9.47 (9.48)	- Loss of $3H_2O$.	$ZnO + 6C$
	180–365	178, 285	2	19.77 (20.89)	- Loss of Cl_2, $3CH_4$	
	365–900	464, 800	2	43.44 (42.67) 72.68 (73.02)	- Loss of $C_{12}H_9N_3O_3$	
$[Cd(H_2L)(H_2O)Cl_2]$	30–160	132	1	3.65 (3.10)	- Loss of H_2O.	$CdO + 4C$
	160–245	217	1	11.83 (12.22)	- Loss of Cl_2.	
	245–480	268	1	24.70 (24.45)	- Loss of $C_{10}H_{21}$.	
	480–900	561, 833	2	33.30 (32.03) 73.48 (71.80)	- Loss of $C_7N_3O_3$.	

* n = number of decomposition steps.

loss of 5.64% (calcd. mass loss 5.90%) is observed in the temperature range of 30 °C to 120 °C, on account of the decomposition of the two uncoordinated water molecules. The last three steps show weight loss of about 69.70% (calcd. mass loss 71.31%) in the range of 120–900 °C, on account of the decomposition of two water, 3/2 Cl_2 and $C_{16}H_{22}N_3O_{2.5}$ molecules.

The $[Mn(H_2L)(H_2O)_2Cl]Cl\cdot 2H_2O$ complex concerned five steps of weight loss, as shown in Table 5. A primal three weight loss

Table 6. BET surface area and band gaps of metal chelates.

Samples	S_{BET} (m^2/g)	Pore volume (cc/g)	Average Particle radius (nm)	BET surface area ($m^2\ g^{-1}$)	Band gap energy (eV)	Average Pore Size (nm)
$[Cr(H_2L)(H_2O)_2Cl]Cl_2\cdot 2H_2O$	119	0.20	7.75	176	3.41	2.28
$[Mn(H_2L)(H_2O)_2Cl]Cl\cdot 2H_2O$	90	0.15	4.32	118	3.41	2.57
$[Fe(H_2L)(H_2O)_2Cl]Cl_2$	13	0.02	5.83	23	3.68	1.95
$[Ni(H_2L)(H_2O)]Cl_2\cdot 4H_2O$	51	0.09	5.32	95	3.14	2.02
$[Cu(H_2L)Cl]Cl\cdot 2H_2O$	79	0.14	8.71	156	3.44	1.73
$[Zn(H_2L)(H_2O)Cl_2]\cdot 2H_2O$	200	0.33	6.10	83	3.69	7.85
$[Cd(H_2L)(H_2O)Cl_2]$	77	0.13	7.96	63	3.66	4.08

of 34.50% (calcd. mass loss 34.81%) is observed in the temperature range of 30 °C to 375 °C, on account of the decomposition of the four water, Cl_2 and C_4H_{10} molecules. The last two steps show weight loss of about 41.62% (calcd. mass loss 42.43%) in the range of 375–900 °C, on account of the decomposition of $C_{12}H_{11}N_3O_3$ molecule.

The $[Fe(H_2L)(H_2O)_2Cl]Cl_2$ complex concerned two steps of weight loss, as shown in Table 5. A total weight loss of 78.15% (calcd. mass loss 77.78%) is observed in the temperature range of 30 °C to 900 °C, on account of the decomposition of the $2H_2O$, Cl_2 and $C_{17}H_{21}N_3O_{2.5}$ molecules.

The $[Ni(H_2L)(H_2O)]Cl_2\cdot 4H_2O$ complex concerned four steps of weight loss (Table 5). A primal two weight loss of 27.29% (calcd. mass loss 26.87%) is observed in the temperature range of 30 °C to 250 °C, on account of the decomposition of the five water and Cl_2 molecules. The last two steps show weight loss of about 50.91% (calcd. mass loss 50.74%) in the range of 250–900 °C, on account of the decomposition of $C_{16}H_{21}N_3O_3$ molecule.

The $[Cu(H_2L)Cl]Cl\cdot 2H_2O$ complex concerned four steps of weight loss (Table 5). A primal weight loss of 6.56% (calcd. mass loss 6.55%) is observed in the temperature range of 30 °C to 135 °C, on account of the decomposition of the two uncoordinated water molecules. The last three steps show weight loss of about 69.02% (calcd. mass loss 70.19%) in the range of 135–900 °C, on account of the decomposition of Cl_2 and $C_{17}H_{21}N_3O_3$ molecules.

The $[Zn(H_2L)(H_2O)Cl_2]\cdot 2H_2O$ complex concerned six steps of weight loss (Table 5). A primal two weight loss of 9.47% (calcd. mass loss 9.48%) is observed in the temperature range of 30 °C to 180 °C, on account of the decomposition of the three water molecules. The next two steps show weight loss of about 19.77% (calcd. mass loss 20.89%) in the range of 180–365 °C, on account of the evolution of Cl_2 and $3CH_4$ molecules. The last two steps show weight loss of about 43.44% (calcd. mass loss 42.67%) in the range of 365–900 °C, on account of the decomposition of $C_{12}H_9N_3O_3$ molecule.

The $[Cd(H_2L)(H_2O)Cl_2]$ complex concerned five decomposition steps as shown in Table 5. A primal weight loss of 3.65% (calcd. mass loss 3.10%) is observed in the temperature range of 30 °C to 160 °C, on account of the decomposition of the one water molecule. The second step shows a weight loss of about 11.83% (calcd. mass loss 12.22%) in the range of 160–245 °C, on account of the evolution of Cl_2 molecule. The third step shows a weight loss of about 24.70% (calcd. mass loss 24.45%) in the range of 245–480 °C, on account of the evolution of $C_{10}H_{21}$ molecule. The last two steps show weight loss of about 33.30% (calcd. mass loss 32.03%) in the range of 480–900 °C, on account of the decomposition of $C_7N_3O_3$. molecule.

The thermograms of the complexes revealed their tentative structures and confirmed the presence of uncoordinated water molecules in all metal complexes except Cd(II) complex.

2.2.10 Mass spectral study

The H_2L ligand mass spectrum showed a molecular ion peak at m/z = 379 amu which matches well with the suggested formula $^{[C21H21N3o4]+}$ with calculated molecular weight of 379.43 g/mole. A molecular ion peak at m/z = 580.5 amu was found in the mass spectrum complex Cd(II), which was coextensive by calculated molecular weight of 580.8 g/mole. Hence, the stoichiometry of this complex is $[Cd(H_2L)(H_2O)Cl_2]$. The peak corresponding to the parent ligand, on the other hand, seemed at m/z 379 amu in the mass spectrum of the Cd(II) complex confirming the complex formation. Figure 6 showed the mass spectra of Schiff base ligand and Cd(II) complex.[14]

2.2.11 BET surface area

The BET measurements (Table 6) were carried out in the direction of determining the surface area of the metal complexes. The obtained data showed high surface area, which was found in the range of 23–176 $m^2\ g^{-1}$. It is to be observed that the high surface area, might be contributed to the mesoporous structure and nano size of the particles with average particle radius of 4.32–8.71 nm.[31] Surface area and pore volume values estimated through nitrogen adsorption isotherms by relative pressures (p/p°) are given in Table 6. The micropore volumes and S_{BET} values of synthesized complexes showed an excessively large decrease in pore volume (0.33–0.02 cc/g) and surface area (200–13 m^2/g).[32]

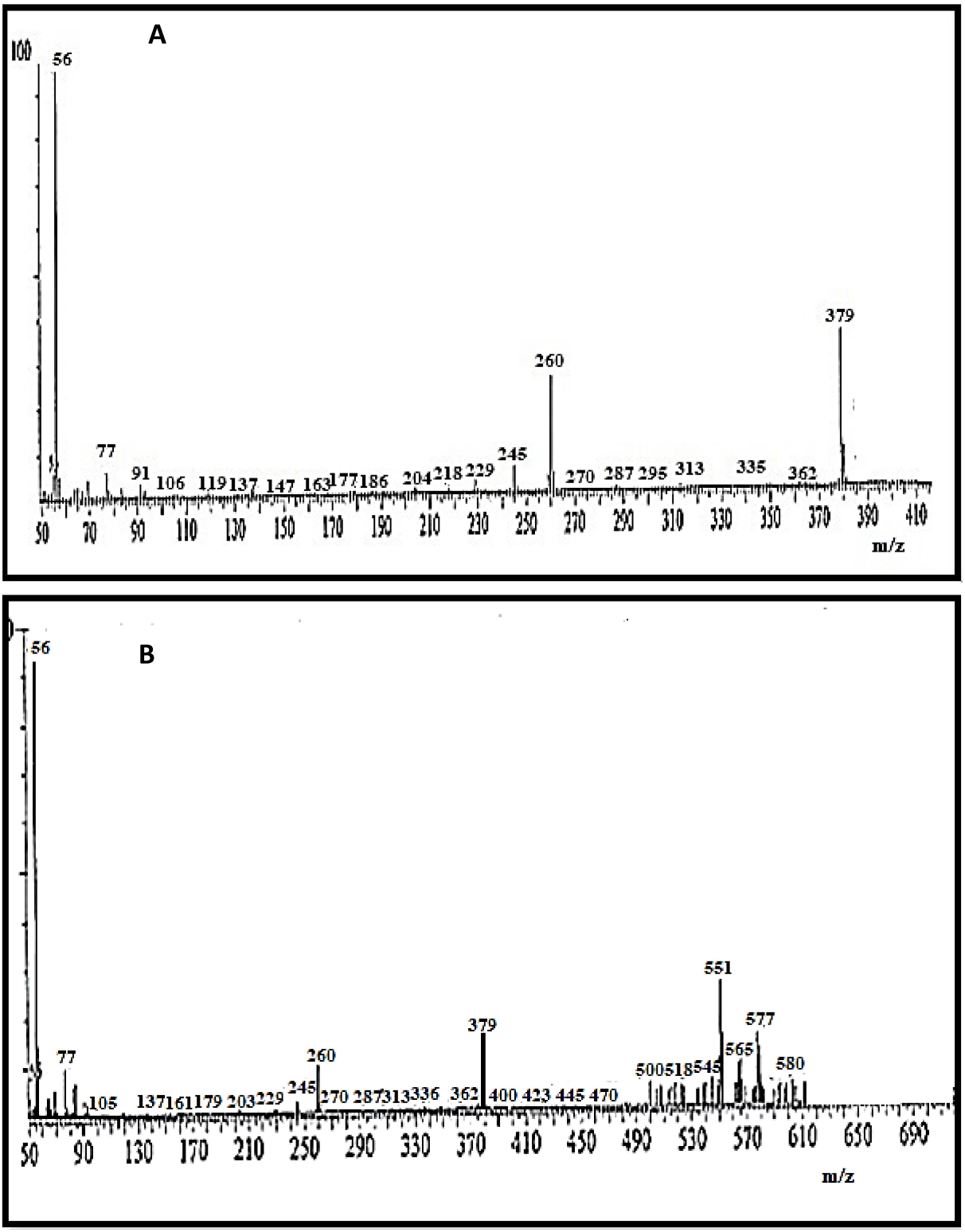

Figure 6. Mass spectra of (A) H_2L ligand and (B) $[Cd(H_2L)(H_2O)Cl_2]$complex.

2.2.12 Antimicrobial assays

An *in-vitro* antibacterial activity outcome of the Schiff base ligand and metal complexes were tested opposed to the Gram-negative (*E. coli*) and the Gram-positive (*S. aureus*) bacterial strains and *in vitro* antifungal activity results opposed to *C. albicans* and *A. flavus* through well diffusion method were studied[33] and the results are shown in Table 7.

Table 7. Biological activity of Schiff base ligand (H_2L) and its metal complexes.

Sample	Inhibition zone diameter (mm/mg sample)			
	Bacterial species		Fungal species	
	G^+	G^-		
	Staphylococcus aureus	*Escherichia coli*	*Aspergillus flavus*	*Candida albicans*
Control: DMSO	0.0	0.0	0.0	0.0
Standard Amikacin Antibacterial agent	10	6	–	–
ketokonazole Antifungal agent	–	–	8	9
H_2L	12	14	0	10
$[Cr(H_2L)(H_2O)_2Cl]Cl_2{\cdot}2H_2O$	9	9	0	0
$[Mn(H_2L)(H_2O)_2Cl]Cl{\cdot}2H_2O$	10	11	0	0
$[Fe(H_2L)(H_2O)_2Cl]Cl_2$	11	13	14	12
$[Ni(H_2L)(H_2O)]Cl_2{\cdot}4H_2O$	16	15	0	19
$[Cu(H_2L)Cl]Cl{\cdot}2H_2O$	14	14	0	0
$[Zn(H_2L)(H_2O)Cl_2]{\cdot}2H_2O$	14	14	0	10
$[Cd(H_2L)(H_2O)Cl_2]$	20	24	11	20

A comparative study of the Schiff base and its complexes reveals a greater antimicrobial activity of the metal complexes than the parent Schiff base ligand (Figure 7). This is because metal chelates are reduced by ligand coordination, which increases their lipophilicity and thus increases the spread of metal ion via the membrane. The chelating effect therefore renders the metal complex like strong antibacterial agents, inhibiting the growth of microorganisms or destroying their active sites.[35,36]

The behavior of the prepared Schiff base ligand and its metal complexes was demonstrated through calculating the activity index using the following relation:

Activity index (A) = Inhibition Zone of compound m /Inhibition Zone of standard drug mm × 100.

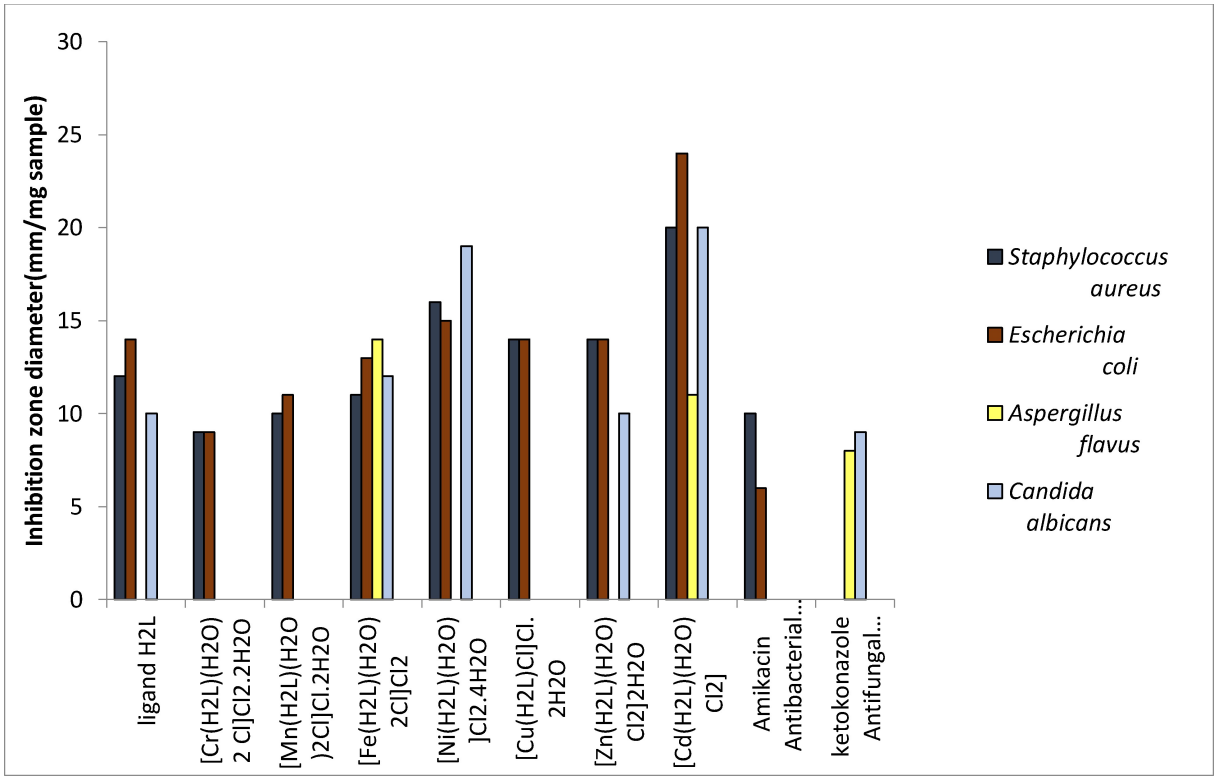

Figure 7. Biological activity of Schiff base ligand (H_2L) and its metal complexes.

The data obtained were shown in Figure 8(a,b). Lastly, the order of rising bacterial and fungal growth inhibitory capacity is in the following order:

For *E. coli*: Cr(III) < Mn(II) < Fe(III) < H_2L=Zn(II) = Cu(II) < Ni(II) - < Cd(II),

For S. aureus: Cr(III) < Mn(II) < Fe(III) < H_2L < Zn(II) = Cu(II) < Ni(II) < Cd(II),

For *Candida albicans*: H_2L=Zn(II) < Fe(III) < Ni(II) < Cd(II)

and For *Aspergillus flavus:* Cd(II) < Fe(III).

Results obtained emphasize that, the metal complexes exhibited higher antimicrobial activity than the free ligand. In addition, the maximum zones of inhibition were obtained in Fe(III) complex with 14 mm zone of inhibition against *Aspergillus flavus*, Cd(II) complex with 20 mm against *S. aureus* and Cd(II) complex with 24 and 20 mm against *E. coli* and *Candida albicans,* respectively.[35]

Just before assess the biological profile, an additional series of antimicrobial agents based on metal complexes of [(1E)-1-(2-hydroxyphenyl)ethylidene]-2-oxo-2H-chromene-3-carbohydrazide Schiff base ligand possessing a NOO donor sites was synthesized and in detail analyzed. Its Cd(II) complex showed the maximum zone of inhibition 18 and 20 mm against *E. coli* and *Staphylococcus aureus* cells compared to reported [Cd-(H_2L)(H_2O)Cl_2] complex which showed nearly the same zone of inhibition 24 and 20 mm against the same organisms.[36,37] For the same Schiff base ligand, Fe(III) complex showed the maximum zone of inhibition 14 mm against *Aspergillus flavus* which is the same to the reported [Fe(H_2L)(H_2O)$_2$Cl]Cl_2 against the same organism.[38]

Also, another series of antimicrobial agents based on metal complexes previously prepared with 2-(((1,5-dimethyl3-oxo-2-phenyl-2,3-dihydro-1H-pyrazol-4-yl)imino)(phenyl)methyl) benzoic acid Schiff base ligand, its Cd(II) complex showed the maximum zone of inhibition (20 mm) against *Candida albicans* which is similar to [Cd(H_2L)(H_2O)Cl_2] complex reported herein.[13]

The metal complexes had the highest antimicrobial activity in contrast with the Schiff base ligand. The difference in activity can account to the difference in nature and coordination sites of the ligand coordinated to metal ions. Chelation also improves the lipophilicity of a metal ion, and the entire rupture in the

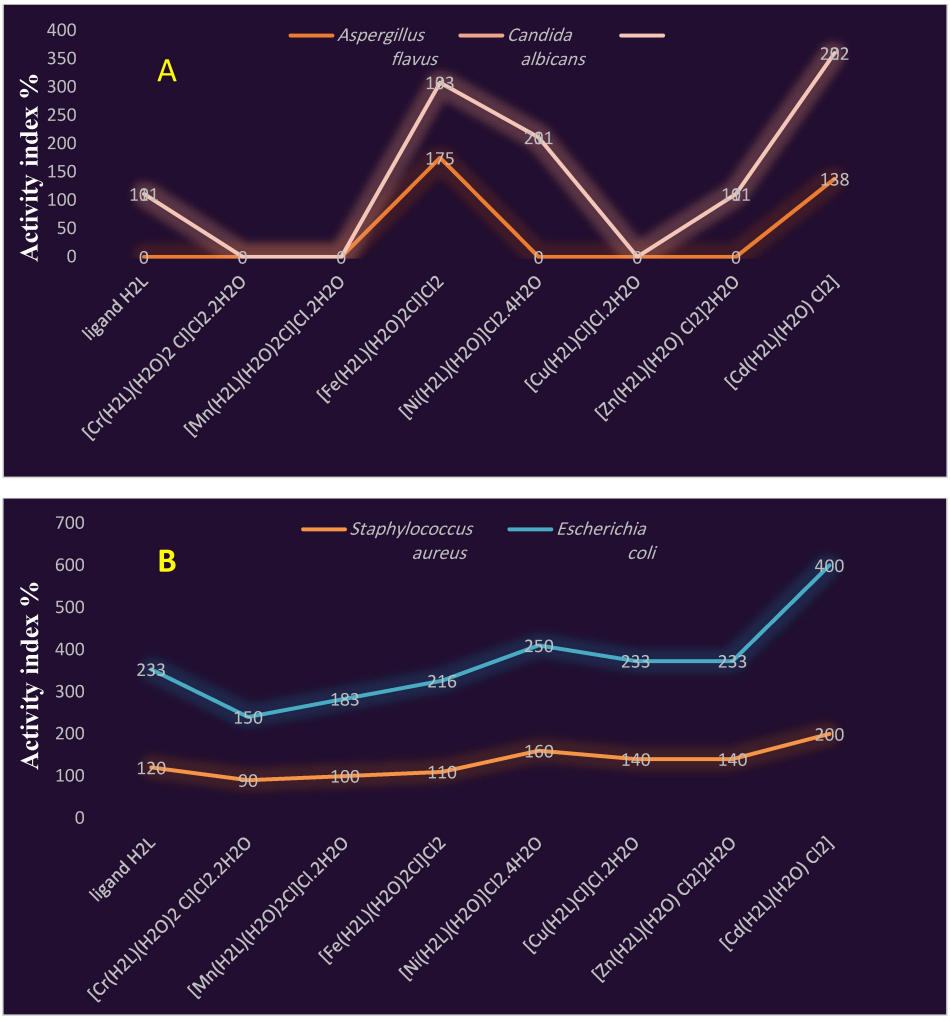

Figure 8. Activity index of Schiff base ligand (H_2L) and its metal complexes against (A) different fungal (B) different Gram (+ ve) and Gram (− ve) bacteria.

cells describes the complete cell rupture as caused by the oxidative stress on the microbial cell entering the nucleus, thus deteriorating the chromosomal DNA through the cellular inhibition of protein synthesis.[36]

2.2.13 Anticancer effects of Schiff base and its complexes

Several concentrations were used to screen the anti-cancer effect of the new Schiff base ligand and its complexes on the human breast carcinoma (MCF-7). Details were provided in Table 8 which provides the anticancer effects of the compounds at 100 μg/ml. The proportion of cell inhibition and IC_{50} values of the complexes have been found to be higher sensitive to the breast cancer cell lines than the free ligand (Figure 9).[33]

The results of the *in vitro* biological test show that the biological activity of metal complexes is greater than that of Schiff base. Furthermore, during the changing of hydrophilicity and lipophilicity, chelation improves the biochemical potential of the bioactive Schiff base, transmitting the cells permeability barriers and speeding the rate of molecules into cell walls. In addition to overloading the metal binding sites in micro-organism enzymes, this type of results increases penetration of metal complexes into lipid membranes. It also distracts the cell's breathing process and blocks the planning of proteins, which limit organisms' supplementary growth.[33]

Comparing the IC_{50} values of Mn(II), Fe(III), Ni(II) and Cu(II) complexes, it can be found that the Cu(II) complex has stronger activity in opposition to human breast cancer cell line (MCF-7) than the other complexes, and its IC_{50} value is 19.6 mg/L. These results gave more possibilities in support of the research and development of metal anticancer drugs and provide some experimental data for the development and application of anticancer drugs. Other than their performance should be further studied,[39] comparable to that of the standard drug cisplatin against MCF-7 cell line cancer cell with $IC_{50} = 2.97$ μg/mL for.[36,37,38]

Table 8. Anticancer effects of Schiff base ligand and its metal complexes in terms of % Cell Inhibition at 100 μg/ml concentration.

Samples	% Cell Inhibition	Surviving fraction (MCF7)					IC_{50} (μg/ml)
		0.0	5.0	12.5	25	50	
H_2L	64						–
$[Cr(H_2L)(H_2O)_2Cl]Cl_2 \cdot 2H_2O$	64						–
$[Mn(H_2L)(H_2O)_2Cl]Cl \cdot 2H_2O$	72	1	0.85	0.73	0.51	0.33	26
$[Fe(H_2L)(H_2O)_2Cl]Cl_2$	75	1	0.88	0.71	0.64	0.25	33
$[Ni(H_2L)(H_2O)]Cl_2 \cdot 4H_2O$	75	1	0.88	0.81	0.62	0.3	34
$[Cu(H_2L)Cl]Cl \cdot 2H_2O$	70	1	1	0.73	0.33	0.31	19.6
$[Zn(H_2L)(H_2O)Cl_2] \cdot 2H_2O$	67						–
$[Cd(H_2L)(H_2O)Cl_2]$	64						–

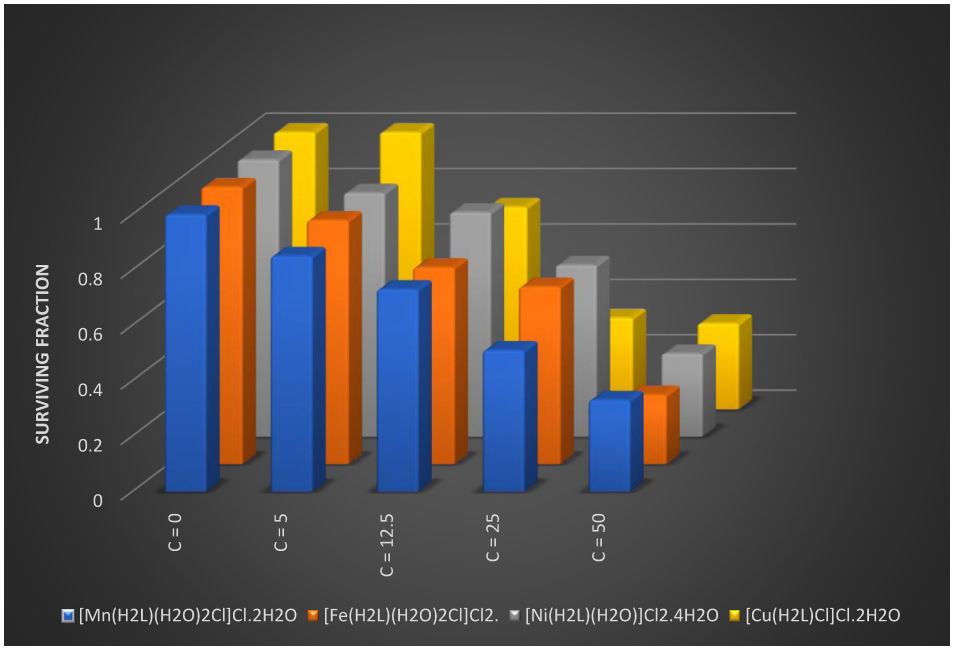

Figure 9. Anticancer effects of Schiff base ligand and its metal complexes in terms of % cell inhibition at 100 μg/ml concentration.

2.2.14 Molecular modeling: Docking study

Computer prediction of the antiviral activity was performed for molecules and drugs used in formularies for the treatment of COVID-19.[42,43] Molecular docking studies have been carried out with the purpose of imagine the binding modes of the H_2L ligand and its metal complexes to crystal structure of the SARS-CoV-2 (COVID-19) main protease in complex by inhibitor UAW247 (6XBH). The lesser most binding energies of the ligand and its metal complexes by 6XBH were calculated and showed in Figure 10. 3D interaction maps showed the binding models of H_2L and its metal complexes towards protein. It was confirmed that wholly the tested compounds were interacted via a hydrogen bond (Table 9 and Figure 10).

After analyzing out the predicted binding conformations of ligand, Cr(III), Mn(II), Fe(III), Ni(II), Cu(II), Zn(II) and Cd(II) complexes with 6XBH docking, the most excellent confirmations exhibited that the free energies of binding (ΔG) were −2.5, −28.6, −3.3, −5.0, −4.9, −3.0, −8.0 and −6.5 kcal/mol, respectively. Ligand, Cr(III), Fe(III) and Ni(II) complexes are binding via H-donor with the amino acid residues of glutamic acid (Glu 166) and methionine (Met 49) except Mn(II), Cu(II), Zn(II) and Cd(II) are binding with the amino acid residues of glutamine (Gln 189), glycine (Gly 143), Glu 166 by H-acceptor with 2.88, 3.38, 3.77, 2.86, 3.31, 3.08, 3.06 and 3.34 A° distances, respectively.[42,43]

The values of interaction energies revealed that its Cr(III) complex had the greatly stable interaction and has a lesser binding energy. Since the point of view of binding energy shows strong interactions with the targets of new coronavirus. This can account to hydrogen bonds formation with the amino acid residues of Met165 and Gln 166. Complex is stabilized by pi-H interactions with the residues of Glu189. [11, 12, 14, 42, 43].

3. Conclusion

The new Schiff base and its complexes were synthesized. The tridentate coordination behavior characteristic to the ligand was evidenced by means of an azomethine nitrogen and two oxygen atoms for all complexes as indicated from the IR spectral studies. The tetrahedral geometry of Ni(II) and Cu(II) complexes and the octahedral geometry of Cr(III), Mn(II), Fe(III), Zn(II) and Cd(II) complexes were inferred from the magnet moment, diffused reflectance and UV-vis spectral studies. The large surface and the small porous size of the BET results of the ligand and its complexes suggested their possible use in different nanotechnology applications. The metal complexes

Table 9. Energy values obtained in docking calculations of H_2L and its metal complexes with to Crystal structure of the SARS-CoV-2 (COVID-19) main protease in complex with inhibitor UAW247 (6XBH).

Compound	moiety	Receptor site	Interaction	Distance (A°)	E (kcal/mol)
Ligand (H_2L)	O 16	OE2 GLU 166	H-donor	2.88	−2.5
	C2 26	SD MET 165	H-donor	3.45	−1.1
	5-ring	NE2 GLN 189	pi-H	3.36	−0.9
$[Cr(H_2L)(H_2O)_2Cl]Cl_2 \cdot 2H_2O$	O15	O THR 24	H-donor	3.09	−1.0
	O54	SD MET 49	H-donor	3.38	−28.6
	6-ring	CG2 THR 25	pi-H	4.55	−0.7
$[Mn(H_2L)(H_2O)_2Cl]Cl \cdot 2H_2O$	O 22	SD MET 165	H-donor	4.03	−0.4
	CL45 49	SD MET 49	H-donor	3.47	−3.1
	O46 50	SD MET 49	H-donor	3.07	−0.9
	O 54	OG1 THR 25	H-donor	2.70	−1.4
	CL45 49	NE2 GLN 189	H-acceptor	3.77	−3.3
	5-ring	CG2 THR 25	pi-H	3.92	−0.7
	6-ring	5-ring HIS 41	pi-pi	3.64	−0.0
$[Fe(H_2L)(H_2O)_2Cl]Cl_2$	O 15	O GLU 166	H-donor	2.86	−5.0
	O 54	OD1 ASN 142	H-donor	2.91	−3.6
$[Ni(H_2L)(H_2O)]Cl_2 \cdot 4H_2O$	O 50	SD MET 49	H-donor	3.31	−4.9
$[Cu(H_2L)Cl]Cl \cdot 2H_2O$	O 15	O ASP 187	H-donor	2.88	−2.9
	CL 50	CG GLN 189	H-acceptor	3.34	−0.8
	CL 50	NE2 GLN 189	H-acceptor	3.08	−3.0
$[Zn(H_2L)(H_2O)Cl_2] \cdot 2H_2O$	CL45 49	CA ASN 142	H-acceptor	4.24	−0.6
	CL46 50	CA ASN 142	H-acceptor	4.03	−0.9
	CL46 50	N GLY 143	H-acceptor	3.06	−8.0
	CL46 50	N CYS 145	H-acceptor	4.27	−1.9
	CL46 50	SG CYS 145	H-acceptor	3.60	−0.9
	6-ring	N GLU 166	pi-H	4.80	−0.7
$[Cd(H_2L)(H_2O)Cl_2]$	O 15	SD MET 165	H-donor	3.51	−2.6
	CL45 49	SG CYS 145	H-donor	3.92	−3.8
	CL45 49	CA MET 165	H-acceptor	3.48	−2.2
	CL45 49	N GLU 166	H-acceptor	4.16	−1.1
	CL46 50	N GLU 166	H-acceptor	3.34	−6.5
	CL46 50	CB GLU 166	H-acceptor	3.64	−0.8

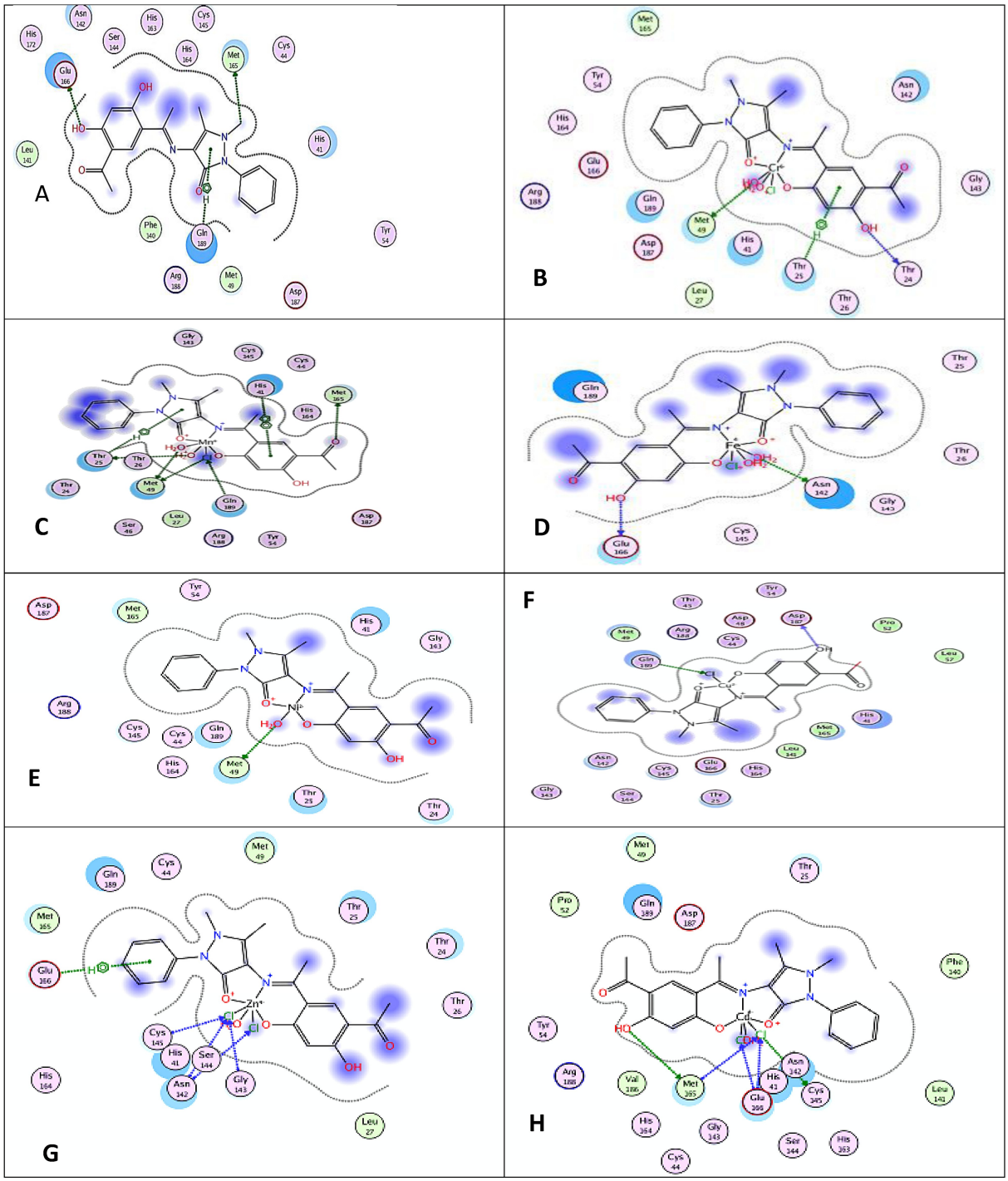

Figure 10. 2D Molecular docking simulation studies of hydrophobic interactions of the Schiff base ligand (A) H_2L and (B) Cr(III), (C) Mn(II), (D) Fe(III), (E) Ni(II), (F) Cu(II), (G) Zn(II) and (H) Cd(II) complexes with amino acid residues of PDB ID: 6XBHare shown with dotteFigure S11. 3D Molecular docking simulation studies of the interaction between (A) Schiff base ligand H_2L and (B) Cr(III), (C) Mn(II), (D) Fe(III), (E) Ni(II), (F) Cu(II), (G) Zn(II) and (H) Cd(II) complexes with the active site of the receptor of PDB ID: 6XBH. The docked conformation of the compound is shown in ball and stick representation

usually showed extra antimicrobial activities than free-ligand molecule which approved the activity of the metal complexes as pathogenic to microorganisms. The recent coronavirus study, H_2L was successful applied in fighting. Its complex Cr(III) has lower binding energy than the ligand, which suggests that antivirals can be strong. This research can lead to new coronavirus treatment in the future.

4. Experimental

4.1. Synthesis of Schiff base ligand and its metal complexes

The novel Schiff base ligand (H_2L) was synthesized through condensation of 4,6-diacetyl-resorcinol (4,6-DAR) and 4-amino-antipyrine. A solution of 4-aminoantipyrine (15.45 mmol, 3.14 g) dissolved in ethanol was added dropwise to 4,6-DAR (15.45 mmol, 3 g) dissolved in DMF. The resulting mixture was stirred in reflux for about 3 h, through which the orange solid compound was separated. It was filtered, recrystallized, washed with diethyl ether and dried in vacuum (Scheme 1).

Complexes of H_2L ligand were synthesized via the reaction of 1:1 molar mixture of warm ethanolic solution (60 °C) of the suitable metal chloride (0.20 g $CrCl_3 \cdot 6H_2O$, 0.15 g $MnCl_2 \cdot 4H_2O$, 0.12 g $FeCl_3 \cdot 6H_2O$, 0.18 g $NiCl_2 \cdot 6H_2O$, 0.13 g $CuCl_2 \cdot 2H_2O$, 0.10 g $ZnCl_2$ and 0.14 g $CdCl_2$; 0.76 mmol) and H_2L (0.3 g, 0.76 mmol). The resulting mixture was stirred under reflux for 1 h whereupon the complexes precipitated. They were collected via filtration and purified through washing several times by diethyl ether.

4.2. Solutions and chemicals

Stock solutions (1×10^{-3} M) of the Schiff base ligand (H_2L) and metal complexes were prepared by precisely weighting the desired quantity and dissolving in DMF solvent. These solutions were utilized for molar conductivity measurement. UV-Vis spectra in DMF solvent within the wavelength range from 200 to 700 nm was measured using dilute solutions of the Schiff base ligand and its metal complexes (1×10^{-4} and 1×10^{-5} M).[13,14]

Chemicals consumed were of the analytical reagent grade (AR) and 4-aminoantipyrine (Sigma) was of the highest purity obtainable. The chemicals consumed included 4,6-diacetyl-resorcinol (Sigma), $CrCl_3 \cdot 6H_2O$, $MnCl_2 \cdot 4H_2O$ and $FeCl_3 \cdot 6H_2O$ (Sigma-Aldrich), $NiCl_2 \cdot 6H_2O$, $CuCl_2 \cdot 2H_2O$ and $ZnCl_2$ (BDH) and $CdCl_2$(Merck). Solvents consumed were ethyl alcohol (95%) and N,N-dimethylformamide (DMF). Bidistilled water was usually consumed in every preparation.[13,14]

4.3 Solution of anticancer study

Stock solution (1×10^{-3} M) of Schiff base ligand in addition to its metal complexes (0.12×10^{-2} g L^{-1}) were prepared in the appropriate volume of DMF (90%). DMSO has been used for cell cryopreservation. The medium RPMI-1640 was prepared as previously described in the protocol of analysis.[13,14]

4.4 Instrumentation

Microanalyses of nitrogen, hydrogen and carbon were approved by the Micro analytical Center, Cairo University, Egypt, via a CHNS-932 (LECO) Vario elemental analyzer. Analyses of the metals content were performed through dissolving the solid complexes in concentrated HNO_3 and dissolving the remnants in deionized water. The metal content was carried out by inductively coupled plasma atomic absorption spectrometry (ICP-AES), Egyptian Petroleum Research Institute. Fourier transform infrared (FT-IR) spectra were recorded with a Perkin-Elmer

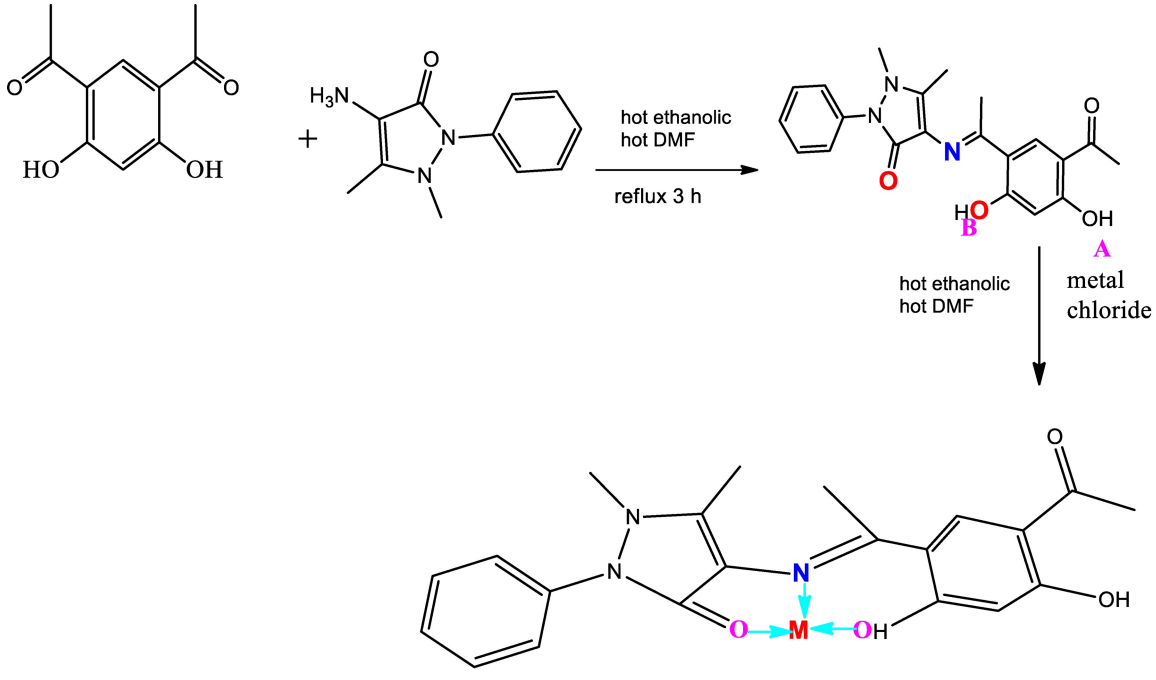

Scheme 1. Preparation of the Schiff base ligand and metal complexes.

1650 spectrometer (400—40 00 cm^{-1}) as KBr pellets. ^1H NMR spectra were carried out in DMSO-d_6 using a 300 MHz Varian-Oxford Mercury instrument at room temperature consuming tetra-methylsilane such as an interior standard. Mass spectra were performed using the electron ionization technique at 70 eV with MS-5988 GS-MS Hewlett-Packard instrument in the Microanalytical Center, National Research Center, Egypt. UV-visible spectra were acquired including a Shimadzu UVmini-1240 spectrophotometer. Molar conductivities of 10^{-3} M solutions of the solid complexes in DMF were measured by a Jenway 4010 conductivity meter. Thermogravimetric analyses (TG) of the solid complexes were carried out from room temperature to 1000 °C by a Shimadzu TG-50H thermal analyzer. Antimicrobial measurements were carried out at the Micro-analytical Center, Cairo University, Egypt. Anticancer activity experiments were performed at National Cancer Institute, Cancer Biology Department, Pharmacology Department, Cairo University. The optical density (OD) of each in good form was measured spectrophotometrically at 564 nm with an ELIZA micro plate reader (Meter tech. R960, Lewiston, USA). The surface area of compounds, gas adsorption measurements, was conducted via N_2 as the adsorptive gas at 77 K. The analysis was carried out via a Nova Touch LX2 analyzer and calculated based on the Brunauer-Emmett-Teller (BET) theory.

4.5 Pharmacology

4.5.1 Antibacterial activities

A modified Kirby-Bauer disc diffusion technique has been used to establish antimicrobial activity of probation samples.[44] The method was followed as fully described in the previously published research.[23] Gram(-ve) bacteria (*Escherichia coli* (ATCC: 11775)), Gram(+ve) bacteria (*Staphylococcus aureus* (ATCC: 12600)) and yeast (*Candida albicans* (ATCC: 7102)) were used. The diameters of the inhibition zones were measured in millimeters. Standard amikacin (antibacterial) and ketoconazole (antifungal) were used as positive controls. The zone diameters were measured by the National Committee for the Pro-Clinical Laboratory Standards' slipping calipers, designed for disaggregation. Agar-based methods such as E-testing and disc diffusion can be alternatives since they are easier and quicker than broth-based methods.[14]

4.5.2 Anticancer activity

The compounds were tested with the method Skehan and Storeng for likely cytotoxicity.[45] For 24 h before the therapy was carried out via the combinations to allow various compound dilution under the analysis of the cell (0, 5, 12.5, 25, 50 and 100 μg/ml) to be mixed into a 96-multiproperly platform to allow the composite to attach to the cell wall of the platform. The monolayer cells, including the compounds 48 hours, were stored warm at 37 °C and 5% CO_2. Cells were fixed and washed after 48 h, with SRB stains stained and stained. The Tris-EDTA buffer washed excess stain with acetic acid and reclaimed stain. ELIZA microplate reader measured the optical density (AD) of all goods spectrophotometrically at 564 nm, average background updates were automatically subtracted, and mean values were calculated of each drug concentration. The relationship between the drug concentration and the surviving fraction is traced into the breast tumor cell line survival curve for each substance. After completion of the protocol, In detail, untreated MCF7 breast cancer cell lines taken as the control group, MCF7 breast cancer cell lines treated with standard drug Cisplatin considered as positive control group. The cell survival percentage was determined as follows:

Survival fraction = O.D (treated cells)/O.D (control cells)

The IC_{50} values (the concentrations of the Schiff base ligand (H_2L) or its metal complexes needed to produce 50% inhibition of cell growth).[14]

4.5.3 Computational methodology

Gaussian09 suite of program was used for the electronic structure calculations of H_2L and Cd(II)complex. DFT based B3LYP method along using the LANL2DZ basis set were employed for full optimization. In order to incorporate the effect of the solvent around the molecule, the TD-DFT method (along with LANL2DZ basic set) was used to estimate the electronic absorption spectra of the ligand and its Cd(II) complex. The contribution of molecular orbital on HOMO and LUMO were also calculated.[14,23]

4.5.4 Molecular docking

Molecular docking studies have been conducted with software MOE2008, to expose the possible binding modes of very good active compounds as opposed to the SARS-CoV-2 (COVID-19) crystal structure, in complex UAW247(PDB ID: 6XBH). It is a steep molecular docking software and is a molecular graphic communication program that allows for the calculation of possible receptor and ligand docking modes and complex molecules. It is also available. The ligand and input receiver in PDB format is required. The sequence of amino acids was reserved and the crystallized ligands, water molecules and chloride ions were deleted. The Crystal structure of the SARS-CoV-2 (COVID-19) was downloaded from the protein data bank (http://www.rcsb.org./pdb).[46]

sh = sharp, m = medium, br = broad, s = small, w = weak

Acknowledgements

The authors wish to share their sincere appreciation to Dr. Walaa H. Mahmoud for the revision of the manuscript.

Conflict of Interest

The authors declare no conflict of interest.

Keywords: Metal complexes · Schiff base ligand · spectroscopic analyses · Microbial and anticancer activity · molecular docking of COVID-19 · density functional theory

[1] M. M. El-ajaily, A. K. Sarangi, R. K. Mohapatra, S. S. Hassan, R. N. Eldaghare, P. K. Mohapatra, T. H. Al-Noor, *Chem. Select.* **2019**, *4*, 9999–10005..
[2] R. K. Mohapatra, M. M. El-ajaily, F. S. Alassbaly, A. K. Sarangi, D. Das, A. A. Maihub, S. F. Ben-Gweirif, A. Mahal, M. Suleiman, L. Perekhoda, M. Azam, T. H. Al-Noor, *Chem. Pap.* **2021**, *75*, 1005–1019.
[3] T. H. Al-Noor, R. K. Mohapatra, M. Azam, L. K. A. Karim, P. K. Mohapatra, A. A. Ibrahim, P. K. Parhi, G. C. Dash, M. M. El-ajaily, S. I. Al-Resayes, M. K. Raval, L. Pintilie, *J. Mol. Struct.* **2021**, 1229, 129832.
[4] A. K. Sarangi, B. B. Mahapatra, R. K. Mohapatra, S. K. Sethy, D. Das, L. Pintilie, M. K. E. Zahan, M. Azam, H. Meher, *Appl. Organomet. Chem.* **2020**, *34*, e5693.
[5] R. K. Mohapatra, P. K. Das, M. K. Pradhan, A. A. Maihub, M. M. El-ajaily, *J. Iran. Chem. Soc.* **2018**, 15, 2193–2227.
[6] F. K. Ommenya, E. A. Nyawade, D. M. Andala, *J. Kinyua. J Chem.* **2020**, *20*, 1745236.
[7] M. Shebl, M. A. El-Ghamry, S. M. E. Khalil, M. A. A. Kishk, *Spectrochim. Acta Part A* **2014**, *126*, 232–241.
[8] K. Dhahagani, M. P. Kesavan, K. G. G. Vinoth, L. Ravi, G. Rajagopal, J. Rajesh, *Mater. Sci. Eng. C* **2018**, *1*, 119–130.
[9] M. Shoaib, G. Rahman, S. W. A. Shah, M. N. Umar, *Bangladesh J. Pharmacol.* **2015**, *10*, 332–336.
[10] R. K. Mohapatra, L. Perekhoda, M. Azam, M. Suleiman, A. K. Sarangi, A. Semenets, L. Pintilie, S. I. Al-Resayes, *J. King Saud Univ.* **2021**, *33*, 101315.
[11] R. K. Mohapatra, S. Mishra, M. Azam, K. Dhama, *De Gruyter.* **2021**, *16*, 491–493.
[12] R. Yu, L. Chen, R. Lan, R. Shen, P. Li, *Int. J. Antimicrob. Agents* **2020**, *56*, 106012.
[13] W. H. Mahmoud, R. G. Deghadi, G. G. Mohamed, *J. Therm. Anal. Calorim.* **2017**, 127, 2149–2171.
[14] W. H. Mahmoud, M. M. Omar, Y. M. Ahmed, G. G. Mohamed, *Appl. Organomet. Chem.* **2020**, *34*, 1–20.
[15] S. M. Abdallah, M. A. Zayed, G. G. Mohamed, *Arab. J. Chem.* **2010**, *3*, 103–113.
[16] W. H. Mahmoud, N. F. Mahmoud, G. G. Mohamed, A. A. El-Bindary, A. Z. El-Sonbati, *J. Mol. Struct.* **2015**, 1086, 266–275.
[17] M. Shebl, M. A. El-ghamry, S. M. E. Khalil, M. A. A. Kishk, *Spectrochim Acta - Part A Mol Biomol Spectrosc.* **2014**, *126*, 232–241.
[18] M. L. Dianu, A. Kriza, N. Stanica, A. M. Musuc, *J. Serb. Chem. Soc.* **2010**, *75*, 1515–1531.
[19] A. J. Abdulghani, R. K. Hussain, *Open J. Inorg. Chem.* **2015**, *5*, 83–101.
[20] W. H. Mahmoud, N. F. Mahmoud, G. G. Mohamed, *J. Therm. Anal. Calorim.* **2018**, *131*, 2775–2793.
[21] A. A. A. Emara, O. M. I. Adly, *Transit Met Chem.* **2007**, *32*, 889–901.
[22] E. V. Sekhar, S. S. Karki, J. Rangaswamy, M. Bhat, S. Kumar, *Beni-Suef University Journal of Basic and Applied Sciences.* **2020**, *13*, 282–290.
[23] Y. M. Ahmed, W. H. Mahmoud, M. M. Omar, G. G. Mohamed, *J. Inorg. Organomet. Polym. Mater.* **2021**, *31*, 2339–2359.
[24] S. Ramarasan, L. R. Sharma, A. N. P. Angelo, *J. Emerging Technologies & Innovative Research.* **2018**, *5*, 394–404.
[25] B. H. Al-Zaidi, M. M. Hasson, A. H. Ismail, *J Appl Pharm Sci.* **2019**, *9*, 45–57.
[26] H. H. Bayoumi, A.N Alaghaz, M.S Aljahdali, *Int. J. Electrochem. Sci.* **2013**, *8*, 9399–9413.
[27] E. Soleimani, *Journal of the Chinese Chemical Society.* **2010**, *57*, 653–658.
[28] M. S. Nair, D. Arish, R. S. Joseyphus, *J. Saudi Chem. Soc.* **2012**, *16*, 83–88.
[29] O. Wahba, A. M. Hassan, A. M. Naser, A. M. Hanafi, *Egypt. J. Chem.* **2017**, *60*, 25–40.
[30] R. Sahu, R. K. Mohapatra, S. I. Al-Resayes, D. Das, P. K. Parhi, S. Rahman, L. Pintilie, M. Kumar, A. Ansari, *J. Saudi Chem. Soc.* **2021**, *25*, 101193.
[31] J. K. Reddy, K. Lalitha, P. V. L. Reddy, G. Sadanandam, M. Subrahmanyam, V. D. Kumari *Catal. Lett.* **2014**, *144*, 340–346.
[32] C. K. Modi, P. M. Trivedi, *Arab. J. Chem.* **2017**, *10*, S1452–1459.
[33] A. Palanimurugan, A. Kulandaisamy, *J. Organomet. Chem.* **2018**, *861*, 263–274.
[34] M. Vairalakshmi, R. Princess, S. Johnsonraja, *Asian J. Pharm. Clin. Res.* **2019**, *12*, 206–210.
[35] G. Sivaprakash, P. Tharmaraj, M. Jothibasu, A. Arun, *Int J Adv Res.* **2017**, *5*, 2656–2663.
[36] M. A. Malik, O. A. Dar, P. Gull, M. Y. Wani, A. A. Hashmi, *MedChemComm* **2018**, *9*, 409.
[37] K. Siddappa, K. Mallikarjun, T. Reddy, M. Mallikarjun, C. V. Reddy, M. Tambe', *J. of Chem.* **2009**, *6*, 615–624.
[38] A. S. Abu-Khadra, A. S. Afify, A. Mohamed, R. S. Farag, H. Y. Aboul-Enein, *The Open Bioactive Compounds J.* **2018**, *6*, 1–10.
[39] Q. Liu, B. Xie, S. Lin, Q. Liao, R. Deng, Y. Zhaohua, *J. Chem. Sci.* **2019**, *131*, 73.
[40] R. S. Mane, A. B. Vedamurthy, *Int. J. Pharma Bio Sci.* **2020**, *11*, 1–6.
[41] A. M. M. Soliman, M. M. Kamel, A. F. Eweas, J. Wietrzyk, M. Milczarek, S. S. Soliman, *Chem. Res. J.* **2018**, *3*, 26–32.
[42] Y. Xu, X. Meng, *Sci. Rep.* **2020**, *10*, 1–13.
[43] U. D. Kamaci, M. Kamaci, A. Peksel, *J. Fluoresc.* **2017**, *27*, 805–17.
[44] A. W. Bauer, W. M. Kirby, J. C. Sherris, M. Turck, *Am. J. Clin. Pathol.* **1966**, *45*, 493–496.
[45] P. Skehan, R. Storeng, *J. Natl. Cancer Inst.* **1990**, *82*, 1107–1112.
[46] ＜Y. M. Ahmed, M.M.Omar· G. G.Mohamed, Journal of the Iranian Chemical Society. 2021,https://doi.org/10.1007/s13738-021-02359-w

Manuscript received: July 25, 2021
Revised manuscript received: September 18, 2021
Accepted manuscript online: September 21, 2021